American Mineralogist, Volume 108, pages 731–737, 2023

Single-crystal X-ray diffraction of fluorapatite to 61 GPa

Melinda J. Rucks[1,*], Gregory J. Finkelstein[1], Dongzhou Zhang[2,3,†], Przemyslaw K. Dera[2,3], and Thomas S. Duffy[1]

[1]Department of Geosciences, Princeton University, Princeton, New Jersey 08544, U.S.A.
[2]Hawaii Institute of Geophysics & Planetology, School of Ocean and Earth Science and Technology, University of Hawaii, Honolulu, Hawaii 96822, U.S.A.
[3]GSECARS, University of Chicago, Building 434A, 9700 South Cass Avenue, Argonne, Illinois 60439, U.S.A.

Abstract

Apatite is a mineral of widespread importance in Earth and planetary science. Here we examine the behavior of a natural fluorapatite (FAp) crystal from Durango (Mexico) under compression to 61 GPa. Single-crystal X-ray diffraction experiments were carried out in a diamond-anvil cell using a synchrotron source. The apatite structure persists up to 32.4 GPa. Birch-Murnaghan equation of state parameters were fit to the pressure-volume data for fluorapatite for two cases: fixing V_0 at its measured ambient value resulted in a bulk modulus, K_{0T}, of 97.0(8) GPa and a pressure derivative of the bulk modulus, K'_{0T}, of 3.3(1), while fixing V_0 and K_{0T} at its ambient value 90.5 GPa (derived from ultrasonically measured elastic constants) resulted in a K'_{0T} value of 4.1(1). At 35.6 GPa, fluorapatite transforms to a triclinic phase ($P\overline{1}$, $Z = 4$), designated here as fluorapatite II (FAp-II). This phase persists up to at least 61 GPa. The major structural differences between FAp and FAp-II involve the buckling of the Ca polyhedra along the *c*-axis and changes in the number and coordination of the Ca sites. Our study extends the pressure range over which fluorapatite has been examined by more than a factor of three, providing new insights into its structural response to high-pressure conditions.

Keywords: Apatite, high-pressure, diamond anvil cell, single-crystal X-ray diffraction

Introduction

Apatite, $Ca_5(PO_4)_3(F,Cl,OH)$, occurs widely in rocky bodies in the solar system, playing an important role as a host for phosphorous and other volatiles. It is one of the most prevalent volatile-bearing phases observed in lunar samples (McCubbin et al. 2010, 2011; Boyce et al. 2014; McCubbin and Jones 2015) and is also found in meteorites (Chen et al. 1995; Sarafian et al. 2013). The apatite structure is highly adaptable and has the ability to incorporate several cations and anions, including Sr^{2+}, Mn^{2+}, Pb^{2+}, Br^{-}, CO_3^{2-}, and rare earth elements (Hughes and Rakovan 2015). Recently, there has been growing interest in the use of apatite as a diagnostic of shock metamorphism in meteorites and at impact sites (Cox et al. 2020; Kenny et al. 2020). This highlights the need for detailed characterization of the behavior of apatite minerals under static and dynamic compression.

Fluorapatite (FAp), $Ca_5(PO_4)_3F$, crystallizes in the hexagonal system (space group $P6_3/m$, $Z = 2$) at ambient conditions (Fig. 1). The structure contains two types of Ca polyhedra, designated Ca1 and Ca2. The Ca1 polyhedron is a tricapped trigonal prism with ninefold coordination. The Ca1 polyhedra share (001) faces and form chains parallel to the *c*-axis. The cations in Ca2 are enclosed in an irregular seven-coordinated polyhedron with six oxygen bonds and one fluorine bond. PO_4 tetrahedra link adjacent Ca1 and Ca2 polyhedra (White and ZhiLi 2003; White et al. 2005). The F anions are located in channels running along the *c*-axis. The cations in the Ca2 polyhedra define a triangle with an F anion at its center with fractional coordinates (0, 0, 1/4). Detailed descriptions of the FAp structure can be found elsewhere (White et al. 2005; Hughes and Rakovan 2015).

The structure and properties of natural apatites have been the subject of extensive study (Hughes 2015; Hughes and Rakovan 2015). An area of interest has centered around the effects of substitution of anions that reside in the halogen site and how solid solution affects the site location (Murayama et al. 1986; Hughes et al. 1989, 2014). Several studies have also been conducted to characterize apatite's structural behavior and phase stability at high pressure (Brunet et al. 1999; Comodi et al. 2001; Matsukage et al. 2004; Konzett and Frost 2009; Konzett et al. 2012; Cámara et al. 2018). Previous studies have shown that fluorapatite persists to 18.3 GPa at room temperature but decomposes into an assemblage containing tuite, γ-$Ca_3(PO_4)_2$, at ~12 GPa and temperatures above 1000 °C (Sugiyama and Tokonami 1987; Matsukage et al. 2004). Natural tuite has been observed in melt veins of shocked meteorites (Baziotis et al. 2013; Xie et al. 2013). To better understand its structural response to compression, we have examined apatite to 61 GPa at ambient temperature using synchrotron-based single-crystal X-ray diffraction techniques.

Experimental methods

A natural, gem-quality crystal of fluorapatite from Cerro de Mercado, Durango, Mexico (Excalibur Minerals) was used in this study. Single-crystal X-ray diffraction at ambient conditions yielded lattice parameters and a unit-cell volume of $a = 9.3937(4)$ Å, $c = 6.8821(3)$ Å, $V = 525.93(5)$ Å^3, where the numbers in parentheses are one standard deviation uncertainties. Microprobe analysis yielded a composition of $(Ca_{5.05}Na_{0.04})(P_{2.93}Si_{0.03}S_{0.02}O_4)_3(F_{0.88}Cl_{0.06}OH_{0.04})$, see Online Materials[1] Table

* E-mail: mrucks@bnl.gov. Orcid 0000-0003-1627-5853
† Orcid 0000-0002-6679-892X

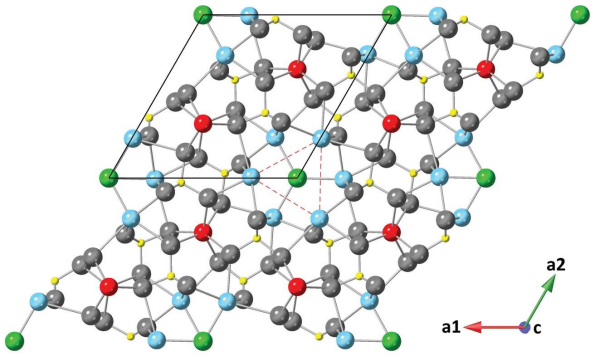

Figure 1. Crystal structure of fluorapatite at ambient conditions. The Ca1, Ca2, P, and F ions are represented as red, blue, yellow, and green spheres, respectively, with oxygen ions in gray. Fluorine anions reside in channels parallel to the *c*-axis formed by Ca2 ions arranged in a triangle, indicated by the dashed red lines. A unit cell is outlined by the solid black line. (Color online.)

OM1. These agree with the literature values for Durango apatite (Hughes et al. 1989; Schouwink et al. 2010; Hovis et al. 2014, 2015). A comparison of unit-cell parameters for the Durango apatite used in this study and other fluorapatite samples is shown in Online Materials[1] Table OM2. A Raman spectrum of the starting material is shown in Online Materials[1] Figure OM1.

A crystal fragment with approximate dimensions 0.018 × 0.018 × 0.008 mm^3 was selected and loaded into a diamond-anvil cell (DAC). The cell incorporated 300 μm diameter culet diamonds backed by Boehler-Almax-type seats with a 70° conical opening (Boehler and De Hantsetters 2004). A sample chamber was created by drilling a ~170 μm hole in a rhenium gasket pre-indented to a thickness of ~33 μm. Two ruby spheres and a fragment of Au foil were included in the sample chamber as pressure calibrants. Helium was loaded into the cell as a pressure-transmitting medium using the GSECARS high-pressure gas loading system (Rivers et al. 2008).

Single-crystal X-ray diffraction experiments at both ambient and high pressure were conducted at the 13-BM-C (PX^2) beamline of the GSECARS sector of the Advanced Photon Source, Argonne National Laboratory (Zhang et al. 2017). Ambient measurements were conducted at the same beamline, outside the DAC, on a separate crystal from the same source as the sample used for the high-pressure experiments. The sample was compressed in ~3 GPa steps using a gas membrane drive. At each compression step, X-ray diffraction data were collected over a 65° angular range along a single rotation axis with a ¼ degree step size and 1 s exposure time per frame. The wavelength of the incident X-ray was 0.4343 Å. The sample-to-detector distance and the orientation of the detector were calibrated using an LaB_6 standard. The data were analyzed using the Bruker APEX3 software. The raw data were processed and integrated using a dynamic mask algorithm to mask blank regions in the Pilatus detector. Absorption corrections were conducted through a scaling step after integration using the SADABS software package. The structure was then solved using SHELXT and refined using the APEX3 refine plug-in based on the ShelXLe engine (Hübschle et al. 2011; Sheldrick 2014). Structure refinements were carried out for all pressures up to 25.8 GPa, and at 43.4 GPa. Anisotropic atomic displacements were used for all but the highest pressure. The CIF are provided in Online Materials[1]. Representative data for an *hk*0 precession image are shown in Online Materials[1] Figure OM2. Ruby fluorescence spectra and Au powder X-ray diffraction patterns were collected before and after the single-crystal diffraction collection at each compression step. Pressures were determined using the [111] reflection of gold using the pressure scale of Fei et al. (2007). The pressures from ruby fluorescence (Mao et al. 1986; Shen et al. 2020) were generally within 1 GPa of the gold values. The ruby lines remained sharp and well separated to maximum pressure, indicating minimal non-hydrostatic stresses.

After reaching the maximum pressure of 61 GPa, the cell was decompressed to 43.4 GPa and removed from the membrane drive to facilitate the collection of additional data for structure refinement. Data were collected at this pressure in phi-scans, for ω values of 0 and 180° at each of three χ positions (–45°, 0°, and 45°). The data collection, in this case, was performed over a 67° angular range on a single rotation axis with a ¼ degree step size, and 2 s exposure time. The structure at this pressure was solved and refined as described above, except that due to limitations in reciprocal space coverage, atomic positions were refined isotropically. Visualization and analysis of the refined structures were carried out using the software CrystalMaker (Palmer 2015).

Results

Analysis of the X-ray diffraction data showed that fluorapatite persists in the $P6_3/m$ structure up to 32.4 GPa at room temperature. This is consistent with previous results from powder X-ray diffraction to 18.3 GPa (Brunet et al. 1999) and Raman spectroscopy to 25 GPa (Williams and Knittle 1996). Representative structure refinements at selected pressures are shown in Table 1. Our results are consistent with previous structure refinements both at ambient and high pressure (Young et al. 1969; Sudarsanan and Young 1978; Hughes et al. 1989; Comodi et al. 2001). It should be noted that for the two compression steps above 25.8 GPa, there was a decrease in the quality of the refinements, as the crystallographic *R* factor (R1) increased to 0.159 at 32.4 GPa relative to the value of 0.036 at 25.8 GPa (Table 1). This is likely due to an increase in crystal mosaicity in this pressure range.

The variation of the unit-cell parameters with pressure for

Table 1. Representative 300 K single-crystal structure refinements and refined atomic parameters for fluorapatite (FAp) at ambient pressure and 25.8 GPa

Beamline	13-BM-C (PX^2), GSECARS, APS, ANL	
P (GPa)	0.0001	25.8
Wavelength (Å)	0.4343	0.4343
T (K)	295	295
Composition[a]	$Ca_5(PO_4)_3F$	$Ca_5(PO_4)_3F$
Symmetry	Hexagonal, $P6_3/m$	Hexagonal, $P6_3/m$
Lattice Parameters: *a*, *b*, *c* (Å)	See Table 2	See Table 2
Volume (Å^3)	See Table 2	See Table 2
Z	2	2
R_{int}	0.0495	0.0371
Reflection range	$-14 \le h \le 14$, $-14 \le k \le 14$, $-10 \le l \le 10$	$-10 \le h \le 6$, $-8 \le k \le 8$, $-7 \le l \le 8$
Maximum 2θ (°)	39	32.5
Total reflections collected	13459	1387
Independent reflections	718	414
Completeness	99.4%	69.7%
Number independent parameters	39	39
Refinement method	F^2	F^2
*R*1	0.0323	0.0363
*wR*2	0.0845	0.0932
Goodness of fit	1.236	1.132

Atom	Site occupancy	*x*/*a*	*y*/*b*	*z*/*c*	U_{iso}
		0.0001 GPa			
Ca1	1	0.666667	0.333333	0.00108(6)	0.00630(14)
Ca2	1	0.99289(4)	0.24202(4)	0.25	0.00504(14)
P1	1	0.36902(5)	0.39845(5)	0.25	0.00220(14)
O1	1	0.48454(17)	0.32689(18)	0.25	0.0071(2)
O2	1	0.46649(18)	0.58795(17)	0.25	0.0090(3)
O3	1	0.25727(12)	0.34203(14)	0.07026(14)	0.0110(2)
F	0.5	0.0	0.0	0.25	0.0200(6)
		25.8 GPa			
Ca1	1	0.666667	0.333333	0.99776(18)	0.0116(3)
Ca2	1	0.98258(10)	0.22328(11)	0.25	0.0062(2)
P1	1	0.37167(14)	0.39808(14)	0.25	0.0050(3)
O1	1	0.4854(4)	0.3144(4)	0.25	0.0119(6)
O2	1	0.4795(4)	0.5967(4)	0.25	0.0192(8)
O3	1	0.2537(3)	0.3412(4)	0.0636(5)	0.0236(7)
F	0.5	0.0	0.0	0.3990(17)	0.028(2)

[a] Nominal. The measured composition was $(Ca_{5.05}Na_{0.04})(P_{2.93}Si_{0.03}S_{0.02}O_4)_3(F_{0.88}Cl_{0.06}OH_{0.04})$.

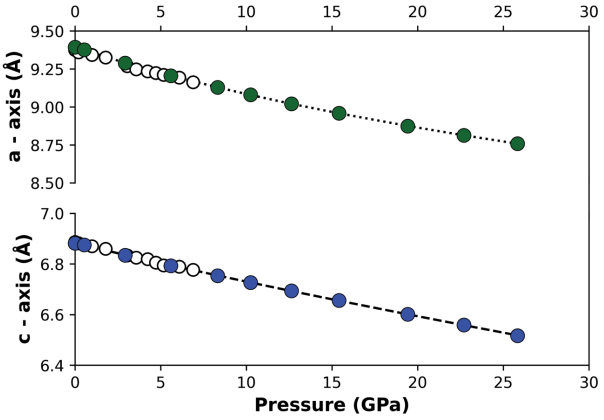

Figure 2. Variation of fluorapatite unit-cell parameters with pressure. Filled circles are from this study (error bars are smaller than the symbol size when not shown) with previous single-crystal data as hollow circles (Comodi et al. 2001). Dashed lines are fits to a linearized Burch-Murnaghan equation. (Color online.)

Table 2. Unit-cell parameters for fluorapatite (FAp)

P (GPa)	*a* (Å)	*c* (Å)	*V* (Å³)
Ambient	9.3937(4)	6.8821(3)	525.93(5)
0.5(1)	9.3768(5)	6.8755(6)	523.53(7)
2.9(1)	9.2892(5)	6.8342(5)	510.71(5)
5.6(1)	9.2059(5)	6.7930(5)	498.57(5)
8.3(1)	9.1290(5)	6.7532(5)	487.40(5)
10.3(1)	9.0972(4)	6.7425(4)	480.27(5)
12.6(1)	9.0214(3)	6.6940(5)	471.81(5)
15.4(1)	8.9584(3)	6.6560(5)	462.60(5)
19.4(2)	8.8736(3)	6.6016(5)	450.17(5)
22.7(1)	8.8132(5)	6.5589(5)	441.19(6)
25.8(1)	8.7588(3)	6.5171(5)	432.99(4)
29.3(4)	8.7018(5)	6.4572(5)	423.44(6)
32.4(1.1)	8.6504(8)	6.3797(9)	413.4(1)

Notes: Error in pressure estimates were calculated through propagating the fit error of the [111] reflection to the final pressure.

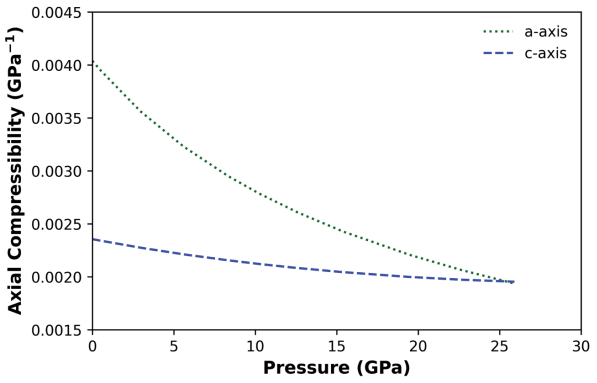

Figure 3. Variation of axial compressibilities of fluorapatite as a function of pressure from the fit to a linearized Birch-Murnaghan equation. (Color online.)

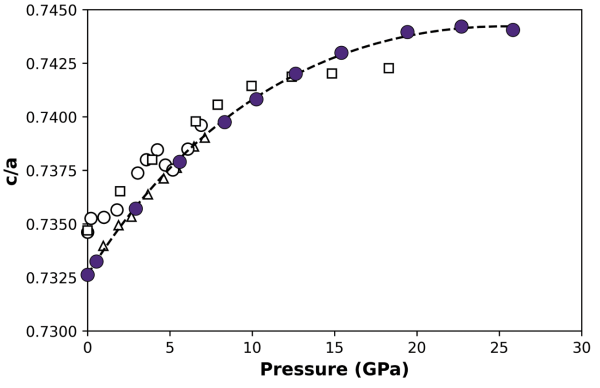

Figure 4. Variation in the *c*/*a* ratio with pressure for fluorapatite. The present data, shown as filled symbols (error bars are smaller than symbol size), are compared to previous studies by Comodi et al. (2001) (hollow circles), Matsukage et al. (2004) (hollow triangles), and Brunet et al. (1999) (hollow squares). (Color online.)

fluorapatite is given in Figure 2 and Table 2. At low pressures, the variation of the axial lengths agrees with an earlier single-crystal study on synthetic fluorapatite (Comodi et al. 2001) (Fig. 2). A linearized Birch-Murnaghan equation was fit to the axial compression data (Xia et al. 1998) (Figs. 2 and 3). The resulting axial moduli, K_{0a} and K_{0c}, and their corresponding pressure derivatives, K'_{0a} and K'_{0c} were: K_{0a} = 82.5(4) GPa, K'_{0a} = 3.80(5), K_{0c} = 141.5(9) GPa, and K'_{0c} = 1.77(8). These results indicate that the *a*-axis is initially much more compressible than the *c*-axis, but the axial compressibilities converge by 25 GPa. This is a consequence of the stiffness of the polyhedral chains along the *c*-axis relative to the compressibility of the anion channels perpendicular to *c* (Sha et al. 1994; Comodi et al. 2001) (Fig. 3). As a result of the differences in axial compressibility, the *c*/*a* ratio initially increases with pressure (Fig. 4), in agreement with previous studies on both single-crystal and polycrystalline samples (Brunet et al. 1999; Comodi et al. 2001; Matsukage et al. 2004). Above ~15 GPa, the *c*/*a* ratio flattens with pressure as the axial compressibilities converge.

The volume compression data were fit with a third-order Burch-Murnaghan equation of state using the EOSfit7c software (Angel et al. 2014). By fixing the ambient volume, V_0, we obtain an isothermal bulk modulus, K_{0T}, of 95.8(4) GPa and a pressure derivative of the bulk modulus, K'_{0T}, of 3.4(1) (Fig. 5). We also performed the fitting by fixing K_{0T} = 90.5 GPa, which is taken from single-crystal elastic constant measurements (Sha et al. 1994), corrected from adiabatic to isothermal conditions. In this case, we obtain K'_{0T} = 4.1(1). The two equations of state provide nearly identical fits to the data. When fit to a second-order Birch-Murnaghan equation the resulting bulk modulus was K_{0T} = 92.3(5) GPa. The variation of unit-cell volume with pressure in our study is generally in agreement with earlier studies to about 10 GPa (Brunet et al. 1999; Comodi et al. 2001; Matsukage et al. 2004), with deviations at higher pressures, likely due to the presence of non-hydrostatic stress in earlier work on polycrystalline samples (Brunet et al. 1999) (Fig. 5). A comparison of our equation of state results with other studies is given in Table 3.

At 35.6 GPa, a change in the diffraction pattern was observed, indicating a phase transition to a new structure (designated here as FAp-II). The new phase persisted upon subsequent compression to the maximum pressure reached of 61 GPa. The diffraction data could be fit to a triclinic unit cell (Table 4), but the diamond-anvil cell and associated membrane drive configuration provided insufficient reciprocal space coverage for a refinement

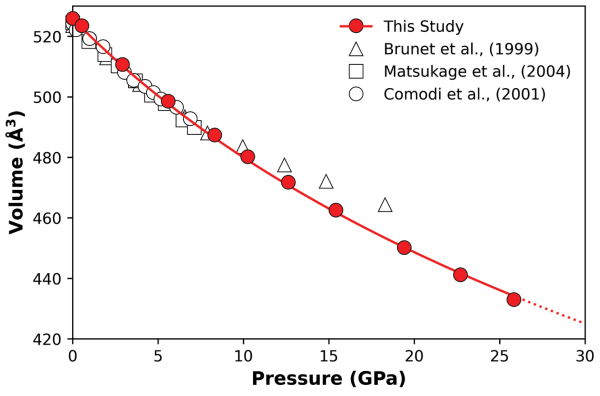

FIGURE 5. Volume vs. pressure for fluorapatite together with a third-order Burch-Murnaghan fits to the data. (Color online.)

of this low-symmetry structure. Consequently, as described in the methods section, after decompressing the cell to 43.4 GPa and removing it from the membrane drive, data were collected at additional χ rotations. This made it possible to perform a structure refinement at this pressure indicating a space group of $P\bar{1}$ (Z = 4), which yielded an R1 value of 0.0537 (Online Materials[1] Table OM3).

In the FAp-II structure, there are 10 Ca sites. These sites can be grouped into two sets that are related to the Ca1 and Ca2 sites in FAp. For simplicity, we refer to these groups of sites as Ca1′ (Ca1A, Ca1B, Ca1C, and Ca1D) and Ca2′ (Ca2A, Ca2B, Ca2C, Ca2D, Ca2E, Ca2F), respectively. In the case of Ca1′, there are four sites, two of which are 8-coordinated (Ca1C and Ca1D) and two are 9-coordinated (Ca1A and Ca1B), which form a column in an 8-8-9-9 arrangement, sharing faces similar to the Ca1 column in the FAp phase. The Ca1′ polyhedral columns are connected through edge and corner sharing with PO_4 tetrahedra (Fig. 6).

TABLE 3. Burch-Murnaghan equation of state parameters

	V_0 (Å³)	K_{0T} (GPa)	K'_{0T}
	FAp		
This study	525.93(5)[a]	95.8(4)	3.4(1)
	525.93(5)[a]	90.5[b]	4.1(1)
	525.93(5)[a]	92.3(5)	4[a]
Comodi et al. (2001)	524.23(5)	93(4)	5.8(1.8)
Matsukage et al. (2004)	524.2(3)	91.5(38)	4.0(11)
	524.2(2)	91.6(10)	4[a]
Brunet et al. (1999)	522.2(4)	97.9(19)	4[a]
	FAp-II		
This study	258(9)	97(19)	4.1[a]

[a] Fixed value.
[b] K_{0T} (fixed) calculated from K_{0S} reported in Sha et al. (1994).

TABLE 4. Unit-cell parameters for fluorapatite-II (FAp-II)

P (GPa)	*a* (Å)	*b* (Å)	*c* (Å)	α (°)	β (°)	γ (°)	*V* (Å³)
35.6(1.5)	8.636(3)	10.648(3)	10.7124(1)	88.407(9)	66.74(2)	66.62(1)	821.0(5)
38.6(1.7)	8.604(3)	10.591(4)	10.664(1)	88.39(1)	66.77(2)	66.62(2)	810.1(5)
41.4(1.7)	8.580(2)	10.534(3)	10.6251(7)	88.349(8)	66.85(2)	66.59(1)	801.0(4)
43.4(1.7)[a]	8.537(4)	10.536(4)	10.622(4)	88.361(5)	66.82(2)	66.54(1)	796.3(6)
44.7(1.8)	8.551(3)	10.479(4)	10.5765(9)	88.32(1)	66.93(2)	66.62(1)	791.4(5)
47.7(1.9)	8.525(2)	10.430(4)	10.533(8)	88.31(1)	67.01(2)	66.66(1)	782.8(5)
50.7(2.1)	8.497(2)	10.387(4)	10.4876(8)	88.313(9)	67.05(2)	66.68(1)	774.1(4)
53.5(1.8)	8.470(3)	10.345(9)	10.447(1)	88.31(2)	67.17(2)	66.72(2)	766.6(8)
55.7(3.0)	8.439(2)	10.305(3)	10.4046(7)	88.28(1)	67.16(2)	66.74(1)	758.0(4)
59.2(3.1)	8.419(2)	10.276(5)	10.3783(9)	88.224(9)	67.15(2)	66.75(1)	752.2(5)
61.0(2.1)	8.403(2)	10.254(4)	10.3536(8)	88.21(1)	67.17(2)	66.75(1)	747.5(5)

Note: See footnote in Table 2 for pressure estimate description.
[a] Data at this pressure was used for the full structure refinement. Sample was partially decompressed from peak pressure (see text for details).

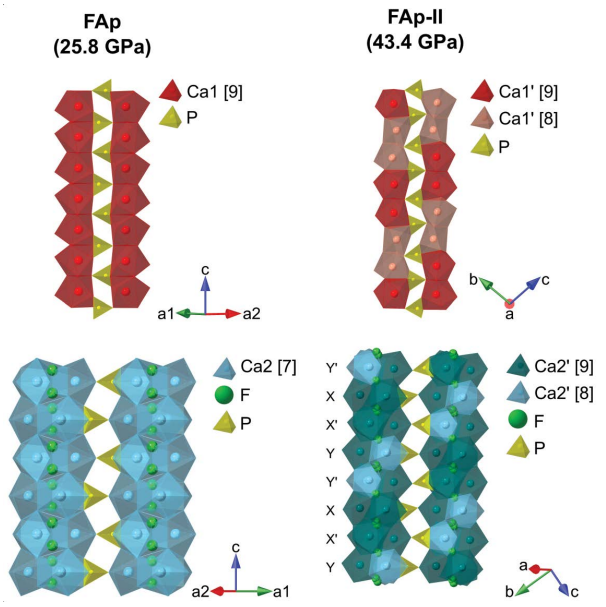

FIGURE 6. Comparison of selected features of the crystal structures of FAp and FAp-II at 25.8 and 43.4 GPa, respectively. (Color online.)

In the case of Ca2′, there are six unique sites, two forming 8-coordinated polyhedra (Ca2A and Ca2B) and four forming 9-coordinated polyhedra (Ca2C, Ca2D, Ca2E, and Ca2F). As in the FAp structure, the Ca2′ cations form layers of Ca2′ site triangles with a central column of F ion sites. In the FAp structure, the Ca2 triangles are translated through a 180° screw axis along the c-axis. This relationship is generally retained in the FAp-II structure, even though the screw axis is absent in the $P\bar{1}$ space group. There are two unique Ca2′ layers, designated here as X and Y, where X is composed of 9 coordinated sites, and Y is a combination of two 8-coordinated sites and one 9-coordinated site (Figs. 6 and 7). The ideal F^- anion sites, of which there are 3 in the FAp-II structure (F1A, F1B, and F1C), are vertically offset such that they appear between the Ca2′ triangle layers. The Ca2′ columns follow a X – F1B – X′ – F1C – Y – F1A – Y′ – F1C arrangement, where X′ and Y′ are the inverse of X and Y (Fig. 7), similar to the screw axis present in the low-pressure structure. In the FAp structure, the Ca2 sites form columns through corner-sharing of the Ca2 polyhedra; in contrast in FAp-II these Ca2′ polyhedral are connected through a combination of face and edge-sharing. Ca2′ sites that are 9-coordinated are face shared with other 9-coordinated Ca2′ sites, and the Ca2′ sites that are 8-coordinated are all edge shared with surrounding Ca2′ polyhedra except for one face, which is shared with a Ca2′ site that is 9-coordinated.

A third-order Burch-Murnaghan equation of state was fit to the volume compression data for FAp-II (Fig. 8). The high-pressure data were fit by fixing the K'_{0T} to the value of 4.1 value obtained from the fits of the FAp structure. The resulting ambient unit-cell volume (V_0) and isothermal bulk modulus (K_{0T}) fit parameters are 258(9) Å³ and 97(19) GPa, respectively (see also Table 3). There is thus little change in the compressibility between the low- and high-pressure phases.

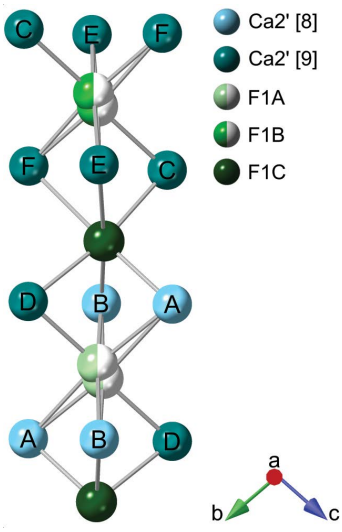

Figure 7. Ca2′ column configuration. F1A, F1B, and F1C indicate the positions of the three ideal fluorine sites. F1A and F1B anions have half occupancy and oscillate between two locations. The Ca2′ configuration involves two 9-coordinated layers (X and X′) and two combined 8- and 9-coordinated layers (Y and Y′). Ca ions are labeled with their letter designation, see Online Materials[1] Table OM3. (Color online.)

Discussion and Implications

Fluorapatite is the most abundant phosphate mineral and has widespread importance in geology. It is a member of the apatite supergroup, a chemically and structurally diverse set of compounds with many important technological applications. An understanding of apatite under compression is of growing interest in light of the increased use of apatite as a diagnostic of impact events. Most previous compression studies of apatites are restricted to relatively low pressures or polycrystalline material, and little is known about how the structure of this mineral or phosphates more generally responds when subjected to more extreme pressures. Our study thus provides new insights into the structural response of fluorapatite as interatomic distances are reduced.

Figure 9 shows the variation in average Ca1-O and Ca2-O bond lengths with compression in FAp. The Ca2 polyhedra become more regular with compression as the relatively long Ca2-O1 bond is highly compressible and becomes similar in length to the Ca2-O3′ bond at 25.8 GPa. Comodi et al. (2001) suggest that the Ca1 polyhedra become more regular with pressure; however, here we observe the opposite, whereby the mean Ca1-O bond distance decreases from 2.554 Å at 1 bar to 2.432 Å at 25.8 GPa, while the standard deviation of the bond distances increases from 0.18 to 0.23 Å. The bond distances in the PO_4 tetrahedra change little with pressure as expected.

A useful metric for understanding the distortion of apatite structures is the metaprism twist angle (φ). The fluorapatite structure can be described in terms of a triangular network of oxygen anions, where the Ca1 site involves regular triangles of O1 and O2, which twist to form these metaprisms (White and ZhiLi 2003; White et al. 2005; Baikie et al. 2007). The twist angle between these O^{2-} triangles can be related to compositional effects (Dong and White 2004a, 2004b; Baikie et al. 2007). Our data at ambient pressure are consistent with typical fluorapatites, which yield φ = 23.3°. Upon compression to 25.8 GPa, we observe an increase in twist angle to 23.9°. We can characterize the distortion of the high-pressure structure through the twist angle of the FAp-II oxygen metaprisms identified as equivalent to those in FAp. The average twist angle for the 8- and 9-coordinated Ca1′ sites are 28.7° and 18.9°, respectively. As discussed in Brunet et al. (1999), the higher twist angles may be correlated with higher

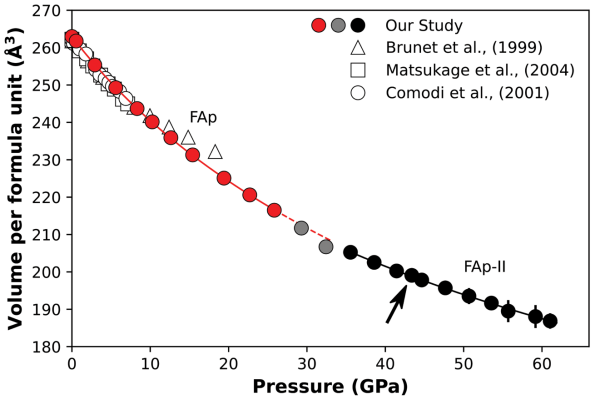

Figure 8. Volume per formula unit of apatite vs. pressure. Third-order Burch-Murnaghan equation of state fits are shown for FAp (red) and FAp-II (black). The gray symbols indicate data for which the quality of the refinement was poor. Arrow indicates datum collected on decompression from peak pressure. (Color online.)

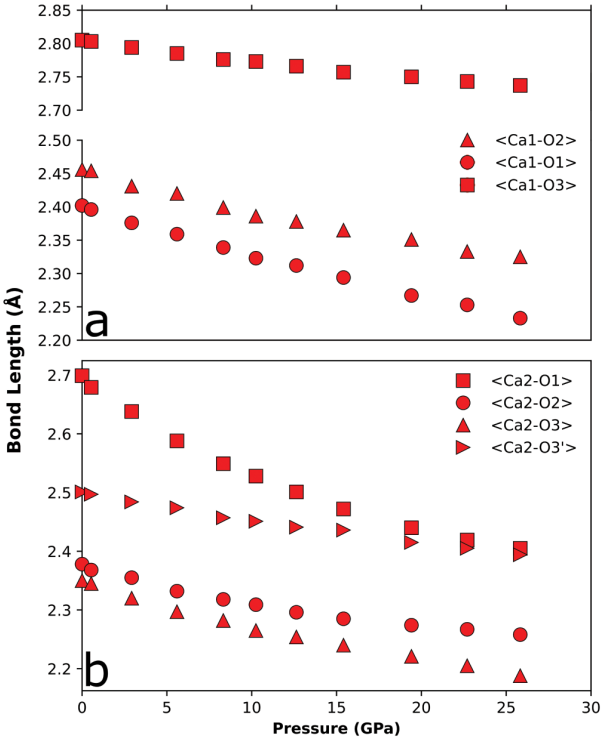

Figure 9. Variation of the average Ca-O bond lengths for anions bonded to Ca1 (**a**) and Ca2 (**b**) in FAp with compression. (Color online.)

stiffness. The large difference in twist angle suggests that in FAP-II the 9-coordinated Ca1′ sites may be more compressible than the 8-coordinated sites.

In end-member fluorapatite, the F anions are in columns along the *c*-axis, located on mirror planes and residing at the center of a triangle defined by three surrounding Ca cations. In natural fluorapatites such as the Durango sample used here, the presence of minor amounts of Cl^- and OH^- substituting for F^- complicates the picture. These ions do not fit well in the center of the Ca triangle and so adopt off-mirror positions along the channel axis. This positional shift can, in turn, displace nearby fluorine ions, leading to the possibility of multiple partially occupied channel anion positions (Hughes et al. 2014).

In our refinements, we assumed an end-member fluorapatite composition as we cannot resolve the presence of minor amounts of other anions. At lower pressures, our results are consistent with the F anion on or near the mirror plane consistent with earlier work (Comodi et al. 2001). However, at pressures above 10 GPa, we observe a strongly increasing elongation of the atomic displacement parameter associated with this site. An important feature of the high-pressure behavior of apatite is the high compressibility of the anion channels normal to the *c*-axis. As a result, the area defined by the Ca triangle decreases strongly with pressure and is reduced by about 25% at 25.8 GPa relative to its ambient value. We postulate that a reduction of the size of the channel with pressure may further drive the F anions away from their ideal position along the *c*-axis. These changes will also lead to corresponding effects on the electrostatic interactions between neighboring channel anions as well as with the surrounding cations under compression. The result would likely be multiple anion positions or disordering that produce the observed large anisotropic displacements and preclude refining the positions as separate sites. Further work is required to better constrain the behavior of the F anion at high pressure.

As far as we are aware, the FAp-II phase is the first report of a triclinic apatite formed under compression. Low-symmetry structures occur in apatites that incorporate cations with relatively large ionic radii into both the polyhedral and tetrahedral sites (White et al. 2005). The transformation from FAp to FAp-II involves collapse along the *c*-axis, as the Ca1 and Ca2 columns can no longer compress without deforming through twisting and buckling of these sites away from the *c*-axis, resulting in the triclinic structure. As can be seen in the structure models (Fig. 6), pseudo-hexagonal symmetry is retained in the triclinic structure. Additionally, as in the FAp structure, we observe disorder of the F^- site (Fig. 7). Two of the three unique F sites are disordered with half occupancy, though our interpretation of these sites is limited as we were unable to achieve refinement of the anisotropic displacement parameters as discussed above.

A major difference between the FAp and FAp-II structures is the change in coordination of the Ca sites. The overall oxygen arrangement around the Ca1/Ca1′ is similar between the FAp and FAp-II structures (Online Materials[1] Fig. OM3). The three O1 and three O2 oxygens are involved in the face sharing of the Ca1/Ca1′ cation polyhedra. In the FAp structure, the Ca1 site has three additional bonds to O3. The decrease in coordination across the phase transition is due to both the kinking away from the *c*-axis shifting of the Ca1 site and distortion of the position and orientation of the PO_4 tetrahedra. These movements pull one oxygen away from the Ca1 site, and it is captured by Ca2 site, changing the coordination of Ca1 from 9- to a combination of 8- and 9-coordinated polyhedra. Additionally, the coordination of the Ca2 site increases from 7 to 8 or 9 in the high-pressure phase.

Acknowledgments and funding

We thank Sergey Tkachev for assistance with gas loading, and Celine Martin for assistance with microprobe data collection at the American Museum of Natural History. This work was supported by the Department of Energy/National Nuclear Security Agency under Cooperative Agreement DE-NA0003957. GeoSoilEnviroCARS is supported by the NSF and the Department of Energy (DOE). Use of the gas loading system was supported by COMPRES and GSECARS. This research used resources of the Advanced Photon Source, a DOE User Facility operated by Argonne National Laboratory.

References cited

Angel, R.J., Alvaro, M., and Gonzalez-Platas, J. (2014) EosFit7c and a Fortran module (library) for equation of state calculations. Zeitschrift für Kristallographie. Crystalline Materials, 229, 405–419, https://doi.org/10.1515/zkri-2013-1711.

Baikie, T., Mercier, P.H.J., Elcombe, M.M., Kim, J.Y., Le Page, Y., Mitchell, L.D., White, T.J., and Whitfield, P.S. (2007) Triclinic apatites. Acta Crystallographica, B63, 251–256, https://doi.org/10.1107/S0108768106053316.

Baziotis, I.P., Liu, Y., DeCarli, P.S., Melosh, H.J., McSween, H.Y., Bodnar, R.J., and Taylor, L.A. (2013) The Tissint Martian meteorite as evidence for the largest impact excavation. Nature Communications, 4, 1404, https://doi.org/10.1038/ncomms2414.

Boehler, R. and De Hantsetters, K. (2004) New anvil designs in diamond-cells. High Pressure Research, 24, 391–396, https://doi.org/10.1080/08957950412331323924.

Boyce, J.W., Tomlinson, S.M., McCubbin, F.M., Greenwood, J.P., and Treiman, A.H. (2014) The lunar apatite paradox. Science, 344, 400–402, https://doi.org/10.1126/science.1250398.

Brunet, F., Allan, D.R., Redfern, S.A.T., Angel, R.J., Miletich, R., Reichmann, H.J., Sergent, J., and Hanfland, M. (1999) Compressibility and thermal expansivity of synthetic apatites, $Ca_5(PO_4)_3$ X with X = OH, F and Cl. European Journal of Mineralogy, 11, 1023–1036, https://doi.org/10.1127/ejm/11/6/1023.

Cámara, F., Curetti, N., Benna, P., Abdu, Y.A., Hawthorne, F.C., and Ferraris, C. (2018) The effect of type-B carbonate content on the elasticity of fluorapatite. Physics and Chemistry of Minerals, 45, 789–800, https://doi.org/10.1007/s00269-018-0962-1.

Chen, M., Wopenka, B., Xie, X., and El Goresy, A. (1995) A new high-pressure polymorph of chlorapatite in the shocked sixiangkou (L6) chondrite. Lunar and Planetary Science Conference XXVI, Abstract 237.

Comodi, P., Liu, Y., Zanazzi, P.F., and Montagnoli, M. (2001) Structural and vibrational behaviour of fluorapatite with pressure. Part I: In situ single-crystal X-ray diffraction investigation. Physics and Chemistry of Minerals, 28, 219–224, https://doi.org/10.1007/s002690100154.

Cox, M.A., Erickson, T.M., Schmieder, M., Christoffersen, R., Ross, D.K., Cavosie, A.J., Bland, P.A., Kring, D.A., and IODP-ICDP Expedition 364 Scientists. (2020) High-resolution microstructural and compositional analyses of shock deformed apatite from the peak ring of the Chicxulub impact crater. Meteoritics & Planetary Science, 55, maps.13541.

Dong, Z. and White, T.J. (2004a) Calcium-lead fluoro-vanadinite apatites. I. Disequilibrium structures. Acta Crystallographica, B60, 138–145, https://doi.org/10.1107/S0108768104001831.

——— (2004b) Calcium-lead fluoro-vanadinite apatites. II. Equilibrium structures. Acta Crystallographica, B60, 146–154, https://doi.org/10.1107/S0108768104001843.

Fei, Y., Ricolleau, A., Frank, M., Mibe, K., Shen, G., and Prakapenka, V. (2007) Toward an internally consistent pressure scale. Proceedings of the National Academy of Sciences, 104, 9182–9186, https://doi.org/10.1073/pnas.0609013104.

Hovis, G.L., Scott, B.T., Altomare, C.M., Leaman, A.R., Morris, M.D., Tomaino, G.P., and McCubbin, F.M. (2014) Thermal expansion of fluorapatite-hydroxylapatite crystalline solutions. American Mineralogist, 99, 2171–2175, https://doi.org/10.2138/am-2014-4914.

Hovis, G., Abraham, T., Hudacek, W., Wildermuth, S., Scott, B., Altomare, C., Medford, A., Conlon, M., Morris, M., Leaman, A., and others. (2015) Thermal expansion of F-Cl apatite crystalline solutions. American Mineralogist, 100, 1040–1046, https://doi.org/10.2138/am-2015-5176.

Hübschle, C.B., Sheldrick, G.M., and Dittrich, B. (2011) ShelXle: A Qt graphical user interface for SHELXL. Journal of Applied Crystallography, 44, 1281–1284, https://doi.org/10.1107/S0021889811043202.

Hughes, J.M. (2015) The many facets of apatite. American Mineralogist, 100, 1033–1039, https://doi.org/10.2138/am-2015-5193.

Hughes, J.M. and Rakovan, J.F. (2015) Structurally robust, chemically diverse: Apatite and apatite supergroup minerals. Elements (Quebec), 11, 165–170,

https://doi.org/10.2113/gselements.11.3.165.
Hughes, J.M., Cameron, M., and Crowley, K.D. (1989) Structural variations in natural F, OH, and Cl apatites. American Mineralogist, 74, 870–876.
Hughes, J.M., Heffernan, K.M., Goldoff, B., and Nekvasil, H. (2014) Cl-rich fluorapatite devoid of OH, from the Three Peaks area, Utah: The first reported structure of natural Cl-rich fluorapatite. Canadian Mineralogist, 52, 643–652, https://doi.org/10.3749/canmin.1400014.
Kenny, G.G., Karlsson, A., Schmieder, M., Whitehouse, M.J., Nemchin, A.A., and Bellucci, J.J. (2020) Recrystallization and chemical changes in apatite in response to hypervelocity impact. Geology, 48, 19–23, https://doi.org/10.1130/G46575.1.
Konzett, J. and Frost, D.J. (2009) The high *P-T* stability of hydroxyl-apatite in natural and simplified MORB—An experimental study to 15 GPa with implications for transport and storage of phosphorus and halogens in subduction zones. Journal of Petrology, 50, 2043–2062, https://doi.org/10.1093/petrology/egp068.
Konzett, J., Rhede, D., and Frost, D.J. (2012) The high *PT* stability of apatite and Cl partitioning between apatite and hydrous potassic phases in peridotite: An experimental study to 19 GPa with implications for the transport of P, Cl and K in the upper mantle. Contributions to Mineralogy and Petrology, 163, 277–296, https://doi.org/10.1007/s00410-011-0672-x.
Mao, H.K., Xu, J., and Bell, P.M. (1986) Calibration of the ruby pressure gauge to 800 kbar under quasi-hydrostatic conditions. Journal of Geophysical Research, 91 (B5), 4673, https://doi.org/10.1029/JB091iB05p04673.
Matsukage, K.N., Ono, S., Kawamoto, T., and Kikegawa, T. (2004) The compressibility of a natural apatite. Physics and Chemistry of Minerals, 31, 580–584, https://doi.org/10.1007/s00269-004-0415-x.
McCubbin, F.M. and Jones, R.H. (2015) Extraterrestrial apatite: Planetary geochemistry to astrobiology. Elements (Quebec), 11, 183–188, https://doi.org/10.2113/gselements.11.3.183.
McCubbin, F.M., Steele, A., Nekvasil, H., Schnieders, A., Rose, T., Fries, M., Carpenter, P.K., and Jolliff, B.L. (2010) Detection of structurally bound hydroxyl in fluorapatite from Apollo Mare basalt 15058,128 using TOF-SIMS. American Mineralogist, 95, 1141–1150, https://doi.org/10.2138/am.2010.3448.
McCubbin, F.M., Jolliff, B.L., Nekvasil, H., Carpenter, P.K., Zeigler, R.A., Steele, A., Elardo, S.M., and Lindsley, D.H. (2011) Fluorine and chlorine abundances in lunar apatite: Implications for heterogeneous distributions of magmatic volatiles in the lunar interior. Geochimica et Cosmochimica Acta, 75, 5073–5093, https://doi.org/10.1016/j.gca.2011.06.017.
Murayama, J.K., Nakai, S., Kato, M., and Kumazawa, M. (1986) A dense polymorph of $Ca_3(PO_4)_2$: A high pressure phase of apatite decomposition and its geochemical significance. Physics of the Earth and Planetary Interiors, 44, 293–303, https://doi.org/10.1016/0031-9201(86)90057-9.
Palmer, D.C. (2015) Visualization and analysis of crystal structures using CrystalMaker software. Zeitschrift für Kristallographie Crystalline Materials, 230, 559–572, https://doi.org/10.1515/zkri-2015-1869.
Rivers, M., Prakapenka, V., Kubo, A., Pullins, C., Holl, C., and Jacobsen, S. (2008) The COMPRES/GSECARS gas-loading system for diamond anvil cells at the Advanced Photon Source. High Pressure Research, 28, 273–292, https://doi.org/10.1080/08957950802333593.
Sarafian, A.R., Roden, M.F., and Patiño-Douce, A.E. (2013) The volatile content of Vesta: Clues from apatite in eucrites. Meteoritics & Planetary Science, 48, 2135–2154, https://doi.org/10.1111/maps.12124.
Schouwink, P., Miletich, R., Ullrich, A., Glasmacher, U.A., Trautmann, C., Neumann, R., and Kohn, B.P. (2010) Ion tracks in apatite at high pressures: The effect of crystallographic track orientation on the elastic properties of fluorapatite under hydrostatic compression. Physics and Chemistry of Minerals, 37, 371–387, https://doi.org/10.1007/s00269-009-0340-0.
Sha, M.C., Li, Z., and Bradt, R.C. (1994) Single-crystal elastic constants of fluorapatite, $Ca_5F(PO_4)_3$. Journal of Applied Physics, 75, 7784–7787, https://doi.org/10.1063/1.357030.
Sheldrick, G. (2014) SHELXT: Integrating space group determination and structure solution. Acta Crystallographica, A70, (a1), C1437, https://doi.org/10.1107/S2053273314085623.
Shen, G., Wang, Y., Dewaele, A., Wu, C., Fratanduono, D.E., Eggert, J., Klotz, S., Dziubek, K.F., Loubeyre, P., Fat'yanov, O.V., and others. (2020) Toward an international practical pressure scale: A proposal for an IPPS ruby gauge (IPPS-Ruby2020). High Pressure Research, 40, 299–314, https://doi.org/10.1080/08957959.2020.1791107.
Sudarsanan, K. and Young, R.A. (1978) Structural interactions of F, Cl and OH in apatites. Acta Crystallographica, B34, 1401–1407, https://doi.org/10.1107/S0567740878005798.
Sugiyama, K. and Tokonami, M. (1987) Structure and crystal chemistry of a dense polymorph of tricalcium phosphate $Ca_3(PO_4)_2$: A host to accommodate large lithophile elements in the earth's mantle. Physics and Chemistry of Minerals, 15, 125–130, https://doi.org/10.1007/BF00308774.
White, T.J. and ZhiLi, D. (2003) Structural derivation and crystal chemistry of apatites. Acta Crystallographica, B59, 1–16, https://doi.org/10.1107/S0108768102019894.
White, T., Ferraris, C., Kim, J., and Madhavi, S. (2005) Apatite—An adaptive framework structure. Reviews in Mineralogy and Geochemistry, 57, 307–401, https://doi.org/10.2138/rmg.2005.57.10.
Williams, Q. and Knittle, E. (1996) Infrared and Raman spectra of $Ca_5(PO_4)_3F_2$-fluorapatite at high pressures: Compression-induced changes in phosphate site and Davydov splittings. Journal of Physics and Chemistry of Solids, 57, 417–422, https://doi.org/10.1016/0022-3697(95)00285-3.
Xia, X., Weidner, D.J., and Zhao, H. (1998) Equation of state of brucite: Single-crystal Brillouin spectroscopy study and polycrystalline pressure-volume-temperature measurement. American Mineralogist, 83, 68–74, https://doi.org/10.2138/am-1998-1-207.
Xie, X., Zhai, S., Chen, M., and Yang, H. (2013) Tuite, γ-$Ca_3(PO_4)_2$, formed by chlorapatite decomposition in a shock vein of the Suizhou L6 chondrite. Meteoritics & Planetary Science, 48, 1515–1523, https://doi.org/10.1111/maps.12143.
Young, E.J., Myers, A.T., Munson, E.L., and Conklin, N.M. (1969) Mineralogy and geochemistry of fluorapatite from Cerro de Mercado, Durango, Mexico. U.S. Geological Survey Professional Paper, 650-D, D84–D93.
Zhang, D., Dera, P.K., Eng, P.J., Stubbs, J.E., Zhang, J.S., Prakapenka, V.B., and Rivers, M.L. (2017) High pressure single crystal diffraction at PX^2. Journal of Visualized Experiments, 119, 54660, https://doi.org/10.3791/54660.

Manuscript received December 9, 2021
Manuscript accepted June 16, 2022
Accepted manuscript online June 30, 2022
Manuscript handled by G. Diego Gatta

Endnote:

[1]Deposit item AM-23-48410, Online Materials. Deposit items are free to all readers and found on the MSA website, via the specific issue's Table of Contents (go to http://www.minsocam.org/MSA/AmMin/TOC/2023/Apr2023_data/Apr2023_data.html). The CIF has been peer-reviewed by our Technical Editors. The structure data (CIF) presented here are also publicly available at the Princeton University DataSpace repository under the following link https://doi.org/10.34770/ark9-b372.